Buried Object Scanning Sonar

Steven G. Schock, *Member, IEEE*, Arnaud Tellier, Jim Wulf, Jason Sara, *Member, IEEE*, and Mark Ericksen

Abstract—A sonar, designed to scan for objects buried in the seafloor, generates images of pipe and cable sections and ordnance buried in sand. The sonar operates by illuminating a broad swath of the seabed using a line array of acoustic projectors while acoustic backscattering from the illuminated sediment volume is measured with a planar hydrophone array. The line transmitter performs along track beamsteering to improve the SNR of buried target images by illuminating major target surfaces at normal incidence and to reduce volume scattering by limiting the volume of sediments illuminated. The output of the planar-hydrophone array undergoes nearfield focusing which allows the sonar to operate near the seabed where target images have the highest SNR and resolution. The nearfield focusing reduces scattering noise by approximately 12 dB, an improvement measured by comparing the SNR of target echoes in single channel data with the SNR of buried targets in the focused imagery. Plan and side views of the seabed generated from a three-dimensional matrix of focused data provide the position and burial depth of targets covered by sand off Hawaii. An energy detector automatically locates targets in the focused image data.

Index Terms—Acoustic imaging, beamforming, buried mine, buried ordnance, buried pipeline, detection, nearfield focusing, reflection profiling, sonar modeling.

I. INTRODUCTION

ACOUSTIC detection of objects buried in the seabed is a much more difficult problem than detection of objects in water due to the high backscattering noise generated by sediments. Acoustic noise in normal incidence-reflection profiles of the seabed is due to volume scattering from inhomogeneities within the sediments, and surface scattering generated by the roughness of sediment–water and sediment layer interfaces. That noise is often higher than the amplitude of echoes reflected from buried targets of interest; consequently, conventional single channel reflection profilers are usually not suitable for finding or imaging buried objects.

Another phenomenon complicating the imaging of buried targets is that the compressional wave attenuation in sediments is much higher than in water. Consequently, subsurface imaging sonars operate at much lower operating frequencies than sidescan sonars, instruments commonly used for generating images of targets in water. As a result, acoustic shadows, which are common in sidescan images of objects lying on the

seabed, are absent in images of buried targets due to diffraction around the target, transmission through the target and relatively high acoustic noise due to backscattering from sediments surrounding the target.

Classification of buried targets is also more difficult since shadows do not exist and since the images do not contain much information about target shape since scattering from oblique target surfaces is not detectable. Acoustic images of buried targets primarily consist of echoes from surfaces of the target that are normal to the incident acoustic ray path. Target surfaces with an oblique aspect to the incident ray path will backscatter much less energy at the lower operating frequencies of subbottom profilers since the acoustic wavelength is much longer than the surface roughness of most targets of interest.

The purpose of this research is to develop a suitable tool for imaging buried objects, such as ordnance, cables, mines, pipelines and archeological sites. Commercial sonars such as multibeam and sidescan sonars usually have arrays oriented in the along track direction and the acoustic axis of the beams are orthogonal to the ship's track. This geometry usually prevents detection of buried objects when major target surfaces are not parallel to the ship's track; e.g., echoes from buried cylindrical objects would usually be undetectable in scattering noise unless the cylinders were oriented in the along track direction.

This paper presents a sonar designed to generate images of buried targets with various aspect angles. The design criteria for the sonar in decreasing order of importance are as follows.

1) Maximize the array gain; that is, maximize the ratio between the echo amplitude and the sediment scattering noise. As the ratio increases so does the image quality and the ability of the sonar to generate images of targets with low target strengths in sediments with high volume scattering. High SNR is also desirable for measuring target signatures using spectral analysis.

2) Design the sonar to maximize the opportunities of illuminating the main surfaces of the target at normal incidence, thereby maintaining high target strengths and minimizing the number of passes at different headings needed to survey the area of interest.

3) Obtain the maximum possible coverage rate without compromising image quality.

4) Maintain array dimensions and electronic packages within a size constraint so the sonar could be deployed on a small vessel or installed on an AUV with a length of approximately 2 m.

5) Provide real time processing and image generation allowing the operator to view the images of buried targets and the x, y and z coordinates of the targets.

6) Provide real time detection of targets to minimize data storage requirements and to allow target data to be viewed
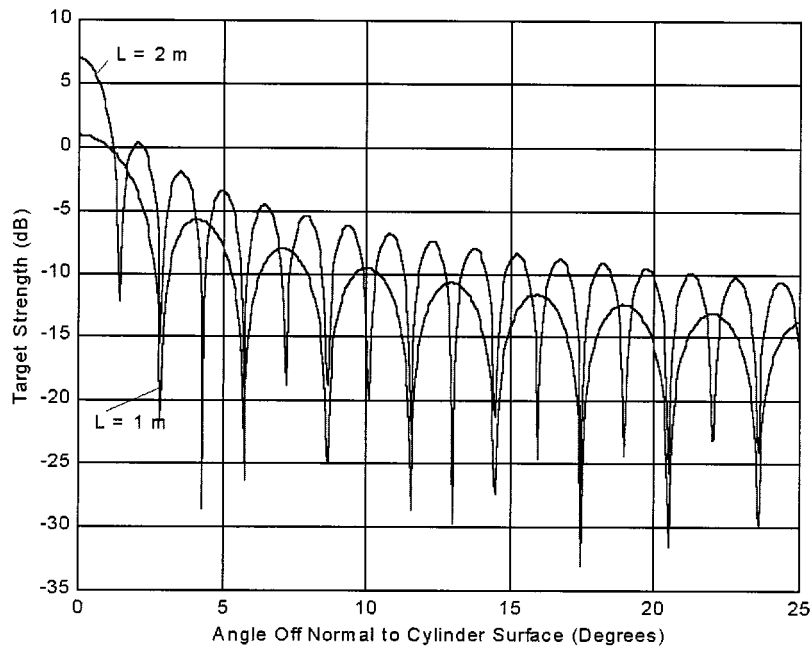
Fig. 1. Target strengths of 50-cm diameter cylinders with lengths of 1 and 2 m at 15 kHz. The aspect angle is measured with respect to the normal to the axis of the cylinder.

and logged immediately or transmitted from an AUV to the support ship via acoustic modem during a survey.

7) Minimize cost and development time by using off the shelf components for constructing the sonar system.

The authors believe that the sonar described in this paper is the first instrument developed to generate real time images of buried objects while allowing for various target aspect angles and providing x, y and z position, size and shape information for buried objects. A sampling of related work includes the use of synthetic aperture sonar for detecting buried targets by NCSC, Panama City, Florida, and Raytheon Company [1], [2]. The synthetic aperture sonars are being developed to detect buried objects near or at the sediment–water interface over wide across track swaths. In order to realize a large search range for detecting buried targets, synthetic aperture sonars must detect those targets at subcritical grazing angles of seabed incidence.

Synthetic aperture sonars designed for buried object detection and the buried object imaging sonar described in this paper can detect echoes from objects buried at subcritical grazing angles under certain conditions. Predicting the performance of a sonar for detecting a target buried outside of the critical angle is difficult because environmental data such as seabed roughness statistics and sediment properties are required by numeric models to make such predictions and that data may not be available or may be changing in a dynamic environment. Recent modeling and experiments indicate that under certain environmental conditions, targets can be detected at subcritical grazing angles when the target is buried near the sediment–water interface in the region of evanescent coupling [3], [4]. Alternative mechanisms for illuminating a target at subcritical grazing angles include the Biot slow wave and scattering caused by the roughness of the sediment–water interface [5], [6]. Simulations using the numerical model OASIS have shown that for subcritical incidence on a rippled seabed, surface roughness can generate much

higher subsurface sound levels than that generated by the Biot slow wave [4].

Simulations of a monostatic sonar using OASIS showed that scattering from a rippled sandy seabed can be much higher than the target echo from a 60-cm diameter solid sphere buried in the region of evanescent coupling at an 18-deg grazing angle [3]. The simulations also showed that varying ripple orientation with respect to the sonar beam can change surface reverberation by as much as 60 dB. Since, for subcritical grazing angles scattering from surficial sediments appears to be the dominant mechanism for illuminating targets below the region of evanescent coupling, seabed roughness statistics including distributions of ripple orientation, height and wavelength, must be known to predict sonar performance for deeply buried targets [3], [5]. Consequently, sonar performance predictions for detecting targets buried below the evanescent coupling region may not be accurate enough to be useful in practice. Since certain targets of interest buried outside the critical angle may not be detectable because of high seabed scattering levels or burial depths below the coupling region, this paper only addresses sonar performance and field experiments for targets buried within the critical angle and sets an effective sonar range that corresponds to a seabed grazing angle that is about 10% greater than the critical grazing angle. Investigations related to subsurface imaging of buried objects inside the critical angle include studies in nearfield focusing [7] and tomographic imaging [8].

II. BACKGROUND

A. Sonar Equations

Sonar equations provide guidelines for system design. The governing equation for the case where volume reverberation noise dominates is given by

$$SL - TL_{\mathrm{i}} - TL_{\mathrm{r}} + TS - RL = SNR\, \mathrm{dB} \qquad (1)$$
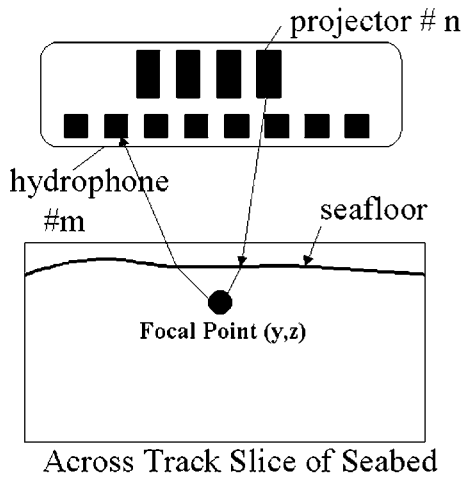
Fig. 2. For each focal point (pixel) in the 2-D across track slice of the seabed, the lengths of the incident and reflected paths are calculated for each hydrophone and projector position to determine the index of the sampled data required for coherent focusing at (y, z) and to determine the spherical spreading correction.
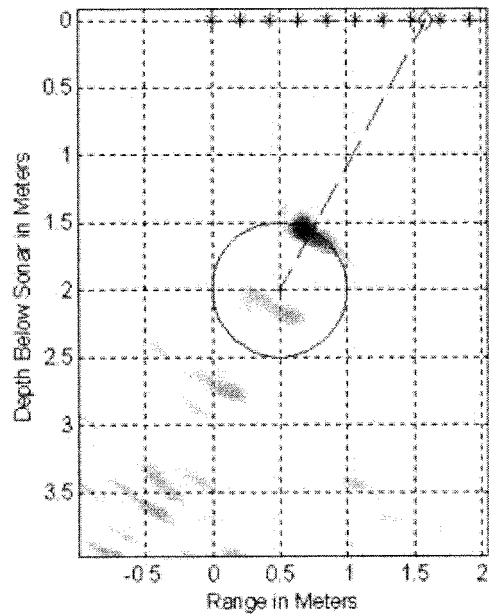

Fig. 3. Synthetic 2-D slice of iron sphere with a diameter of 1 m submerged in water. The image was generated by processing 16 channels of synthetic hydrophone data generated by a point acoustic source located at the center of the hydrophone array.
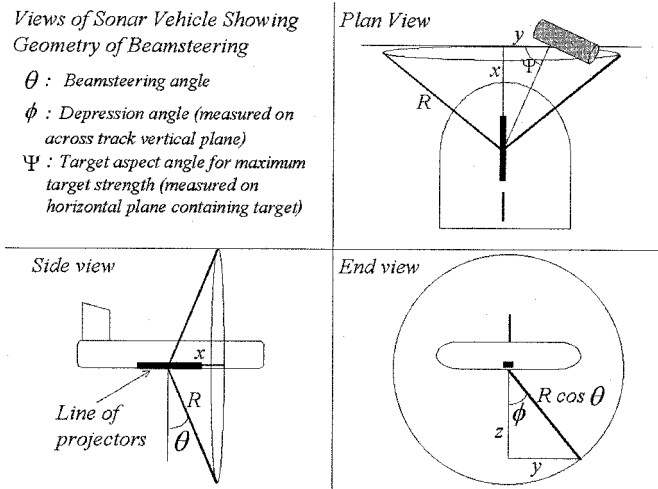

Fig. 4. Geometry used in discussions on beamsteering and angle of target incidence. The line of projectors lies along the axis of symmetry for the conical transmission beam.

where

SL source level;
TL_i transmission loss of the incident wave;
TL_r transmission loss of the reflected echo;
TS target strength;
RL reverberation level of sediments;
SNR signal-to-noise ratio of the sonar data.

The transmission losses of the incident and reflected waves, TL_i and TL_r, account for spherical spreading, acoustic attenuation and boundary losses. The reverberation level due to volume scattering is given by

$$RL = SL - TL_i - TL_r + S_v + 10 \log V \text{ dB} \qquad (2)$$

where

$$V = \frac{c\tau}{2} \Psi r^2 \text{ m}^3 \qquad (3)$$

is the volume of sediment illuminated at an instant in time by the processed acoustic pulse, and

c sound speed;
τ length of the processed pulse;
Ψ effective width in steradians of the two-way system beam illuminating the sediments;
r range from the source to the center of the scatterers.

The volume scattering coefficient of the sediments, S_v, is given by

$$S_v = 10 \log \frac{I_s}{I_i} \qquad (4)$$

where I_i is the intensity of the incident acoustic wave and I_s is the intensity of the signal backscattered per cubic meter of sediment, illuminated at an instant in time, measured in the farfield of the scatterers and referenced 1 m from the scattering center [9], [10].

The most important design criterion for the buried object scanning sonar is to maximize the SNR, the target echo to scattering noise ratio in decibels. Equations(1)–(3) show that

for a target at range r, SNR is improved by reducing the beamwidth Ψ and/or reducing the processed pulse length τ. The system beamwidth can be reduced by increasing array size or increasing the operating frequency. Since reverberation level is proportional to the width of the zero-phase wavelet (the processed FM pulse), and the wavelet width is inversely proportional to the sonar bandwidth, volume scattering can also be reduced by increasing sonar bandwidth. The sonar described in this paper uses an unusually wide bandwidth to minimize scattering noise.

An additional consideration for minimizing reverberation noise is the number of array elements used to construct the array. The SNR of reflection data at the output of a discrete
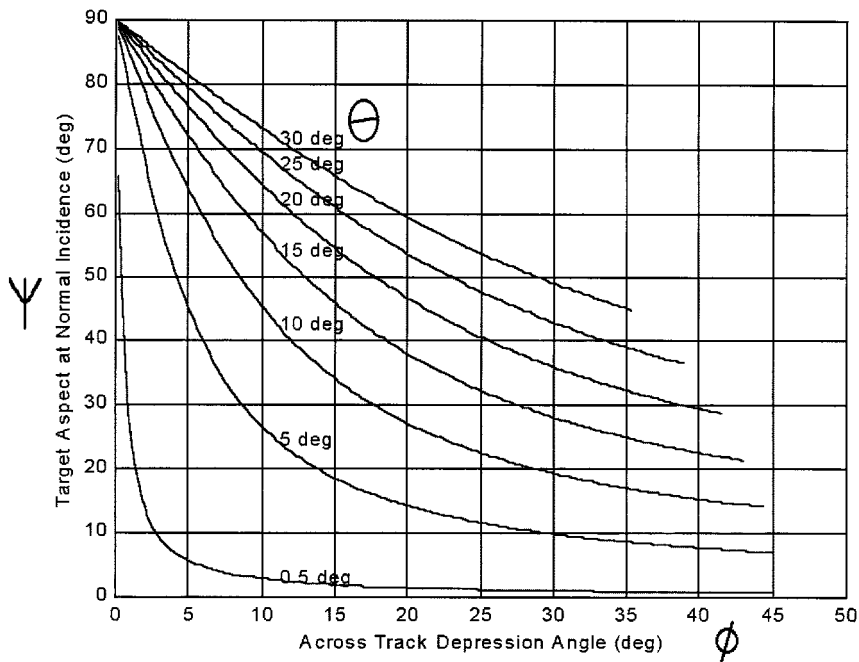
Fig. 5.   Angle of target incidence versus across track depression angle. Each curve represents one steering angle of the transmission beam. The curve ends when the angle of seabed incidence equals 45 deg. The target strength will be the highest when the angle of target incidence equals the target aspect angle.
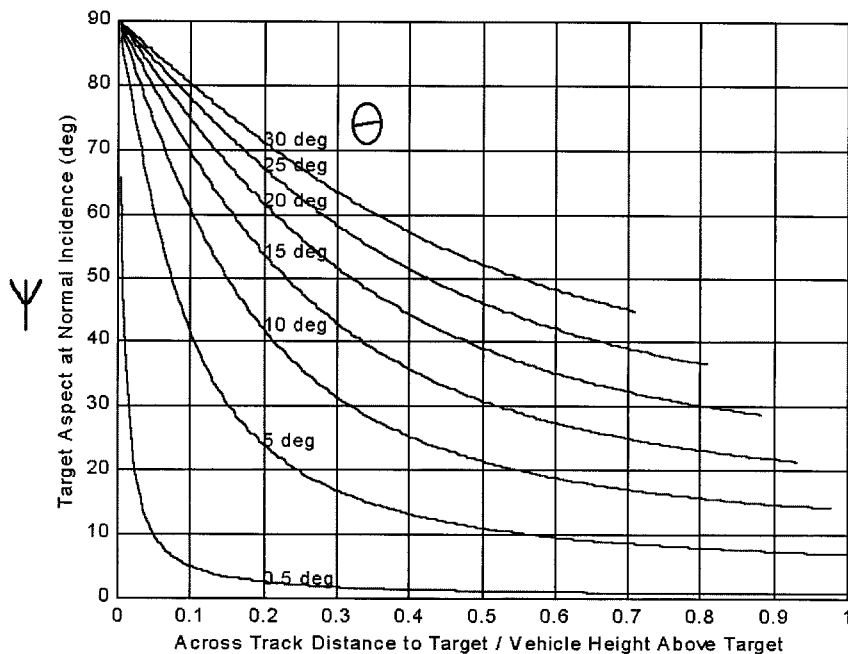

Fig. 6.   Angle of target incidence versus the across track range target to vehicle height ratio. Each curve represents one steering angle of the transmission beam. The curve ends when the angle of seabed incidence equals 45 deg.

element array for the case of a perfectly coherent signal in perfectly incoherent noise improves with the number of elements N according to $10 \log N$ dB. This rule of thumb assumes the element spacing is sufficient so that the cross correlation coefficient of the output between any two array elements is zero [9]. We selected 32 channels in the sonar design which appeared to be a breakpoint in the tradeoff between SNR improvement and the increased complexity and cost of the added hardware and software needed for processing additional channels.

B. Target Strength Versus Aspect

An approximation for the target strength of a rigid finite length cylinder [9] is given by

$$TS = 10 \log \left[\frac{aL^2}{2\lambda} \left(\frac{\sin \alpha}{\alpha} \right)^2 \cos^2 (\gamma) \right]$$

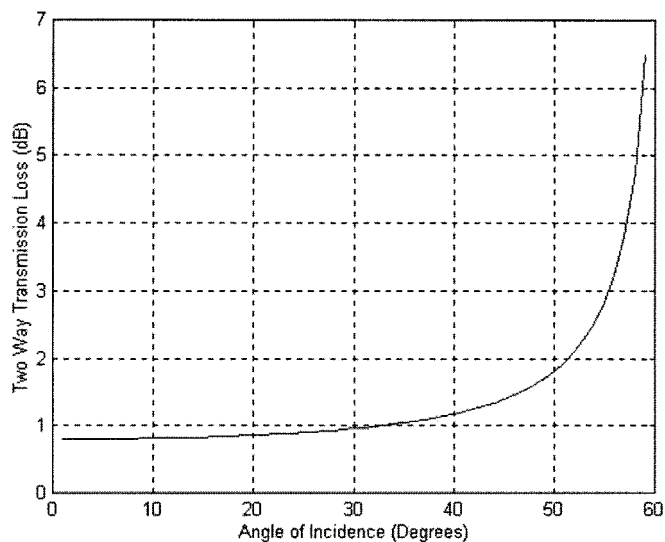$$ka \gg 1, \quad r > \frac{L^2}{\lambda} \tag{5}$$

Fig. 7. Two-way transmission loss versus angle of incidence for a fine sand with a sound speed of 1730 m/s and a density of 1640 kg/cu·m. This figure is calculated using a simple fluid–fluid model [14] for transmission through the sediment–water interface, neglecting the effects of the poro-elastic medium.

where

$$\alpha = kL\sin(\gamma) \qquad (6)$$

a	radius;
L	length;
λ	wavelength;
k	wavenumber;
r	range.

The target strength as a function of the angle γ off the normal to a 50-cm diameter cylinder is plotted in Fig. 1 for a frequency of 15 kHz. The plot shows that one can expect a rapid drop in target strength if the normal to the axis of the cylinder is misaligned with the acoustic axis of the main lobe in the system beampattern. Referring to Fig. 1, the TS can drop atleast 6 dB with a 1-deg change in the cylinder aspect. High sensitivity to target aspect can be reduced by increasing the acoustic beamwidth. Widening the acoustic beamwidth allows an off-axis portion of the main lobe to illuminate the target at normal incidence to the target surface, but at the expense of increased scattering noise and reduced spatial resolution. A solution to this problem is to use a narrow-system beamwidth and to steer the beam to illuminate the targets at various aspects, thereby maintaining low scattering interference, good spatial resolution and high target strength. The sonar described in this paper steers both transmission and reception beams to achieve that effect.

C. Nearfield Focusing

Scattering noise measured at the output of the hydrophone array is a function of the array gain. The array gain is maximum when the received signal is perfectly coherent and the noise is perfectly incoherent between any two channels. To achieve perfect signal coherence, the phase and amplitude of the echo signal from a target must be identical for all data channels before summing the channels. Since the sonar is towed near the seabed to minimize scattering noise, targets are commonly within the

nearfield of the sonar arrays. To achieve perfect signal coherence, one must time shift each of the data channels so the signals add coherently for a reflection emanating from a point scatterer. This focusing process is achieved by delaying the data from each channel according to the differences in travel times from a focal point to the individual receivers.

The expression for nearfield focusing for a sonar with M projectors and N receivers (Fig. 2) is given by

$$A(y,z) = \left| \sum_{n}^{N} \sum_{m}^{M} c_{nm}(y,z) a_{nm}(y,z) \right| \qquad (7)$$

where

$A(y,z)$ amplitude of the image pixel at coordinate (y,z) within the slice of the seabed generated by one transmission event;

$a_{nm}(y,z)$ value of the analytic signal sampled at the arrival time of sound from point (y,z) for the two way path from transducer m to the focal point at (y,z) to hydrophone n;

$c_{nm}(y,z)$ corresponding weighting coefficient that corrects for two way spherical spreading, boundary losses, and attenuation [11].

The coefficients are stored in a lookup table which is updated in real time as the sonar vehicle pitches and rolls. Corrections to the lookup table for refraction and the change of sound speed at the sediment–water interface are described in [12]. Lookup table corrections for refraction were not used for the experiment described in this paper because targets were buried under approximately 30 cm of sand, a burial depth resulting in short subsurface ray path lengths and small phase errors that do not affect imagery. For a vehicle height of 3 m and a sand phase velocity of 1700 m/s, the maximum phase error is about one tenth of a wavelength for a target buried 30 cm in sand within a 110-deg seabed swath measured with respect to the center of the sonar array.

D. Simulated Images of Targets

To gain an understanding of the appearance of buried targets in vertical image slices of the seabed, we generated images of targets by creating synthetic data sets for each of the acoustic receiving channels, passing the synthetic data through the near field focuser and displaying two-dimensional (2-D) slices of the target. A synthetic acoustic return for each channel is generated by convolving the acoustic pulse with the exact analytical expression for the impulse response of the target. The synthetic data are processed by the nearfield focuser, executing (7), to obtain a 2-D slice of the target [11]. Fig. 3 displays the 2-D slice of an iron sphere in water. The image shows that the only significant target echo emanates from the point on the surface of the sphere which has a normal passing through the acoustic projector [13]. No other part of the spherical surface appears in the image. Low amplitude echoes in the image are due to target ringing and diffraction that depend on target shape and material properties. There will be no measurable energy reflected from any other part of the sphere's surface, so the shape of image will not have a spherical appearance, but will appear as a point
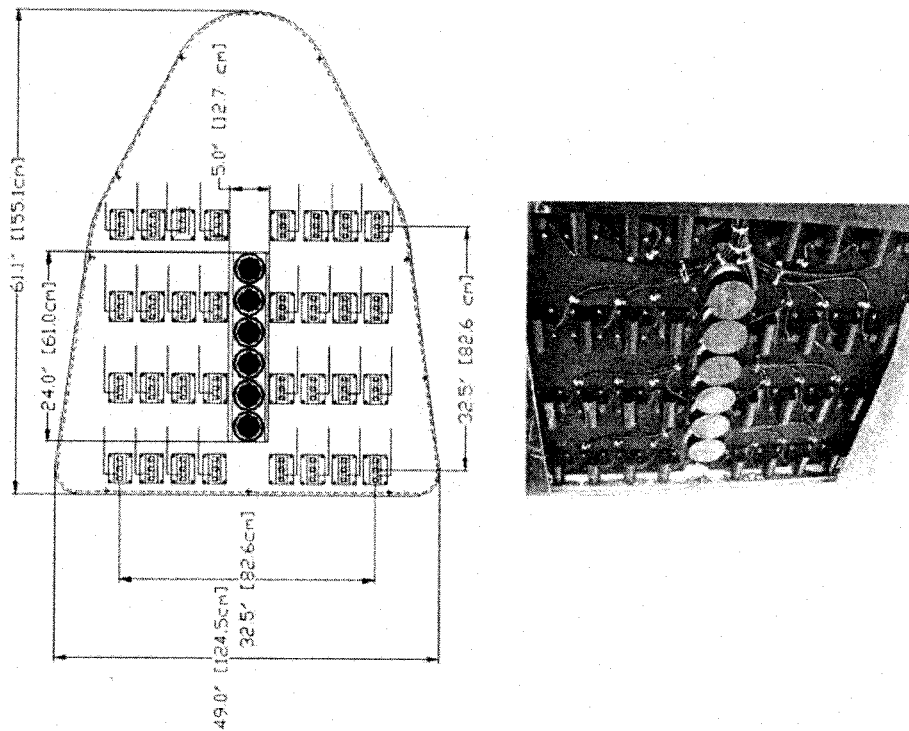
Fig. 8.   Bottom view of sonar vehicle (drawing and photo) showing a line of six projectors and a 32-channel planar hydrophone array consisting of eight rows with four hydrophone channels in each row.

reflector. In general, the reflected echoes originate from the surfaces of targets that are orthogonal to the incident ray path.

III. SONAR SYSTEM DESCRIPTION

A. Target Aspect Considerations in System Design

The buried object scanning sonar design was developed using the design criteria listed in Section I. The final design included a line array of piston projectors oriented along the centerline of the vehicle. The transmission array provides directivity to reduce the volume of sediment illuminated and is used to steer the transmission beam in order to illuminate objects at various aspect angles. The transmission beam is steered by adjusting the transmission delays between successive transducers. Sweeping the conically shaped transmission beam back and forth along track allows targets to be illuminated at various aspects. The geometry of the transmission beam is shown in Fig. 4.

From Fig. 4, one can determine the relationship between the angle of seabed incidence, the transmission angle, the depression angle and the angle of target incidence. The angle of target incidence is the angle in the horizontal plane between a vector passing through the target in the horizontal plane in the across track direction and a vector formed by the intersection of the conical beam and the horizontal plane containing the target. The angle of target incidence, which is plotted against the across depression angle in Fig. 5, is calculated using

$$\tan \Psi = \frac{\tan \theta}{\sin \phi}. \tag{8}$$

The angle of target incidence is plotted against the range to height ratio in Fig. 6 using the expression

$$\frac{\text{across track range}}{\text{vehicle height}} = \frac{y}{z} = \tan \phi. \tag{9}$$

The angle of seabed incidence β is varied from 0 to 45 deg to generate the curves in Figs. 5 and 6, using the expression

$$\cos \beta = \frac{z}{R} = \cos \theta \cos \phi. \tag{10}$$

As shown in Fig. 7, the two-way transmission loss through the sediment water interface increases rapidly above an angle of seabed incidence of 50 deg for fine sand. High two-way transmission loss at large angles of incidence limits the effective across track coverage, or swath width, of the sonar to approximately twice the vehicle height above a sandy seabed. Snell's Law can be used to estimate swath coverage given the seabed sound speed.

The curves in Fig. 6 show the tradeoff between sonar range and the range of aspect angles for target surfaces that are normal to the incident beam. As shown in Fig. 6, all targets passing under the sonar have desirable aspects. As the across track range increases, fewer target surfaces are normal to the transmission beam at a given across track range. Consequently, increasing the across coverage requires steering the transmission beam over a greater range of angles. However, the range of steering angles is limited by the high two way transmission loss when the angle of seabed incidence approaches the critical angle as shown in Fig. 7.
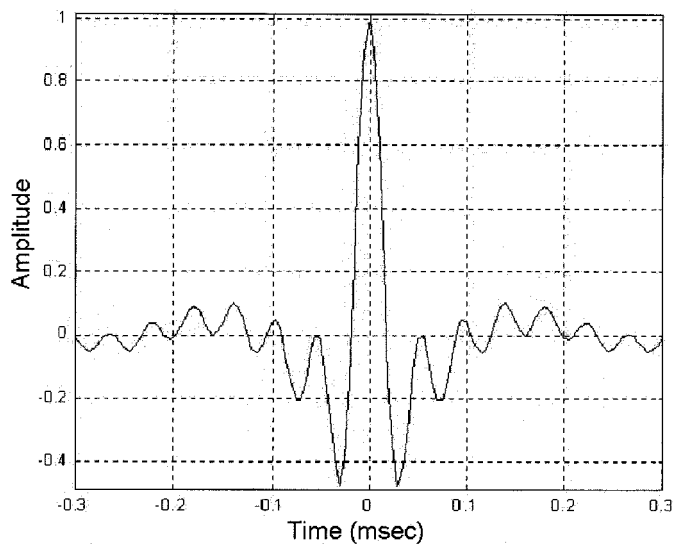
Fig. 9. A zero-phase wavelet is the output of the correlation processor when the input is a 2 ms FM pulse with the spectrum shown in Fig. 10.
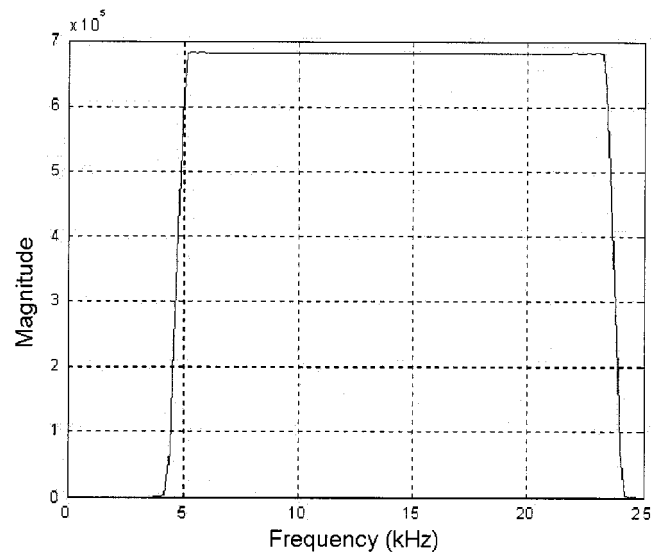

Fig. 10. Spectrum of processed FM signal. The operating band is flat over the band of 5 to 23 kHz as measured at the output of the correlation processor.

B. Acoustic Arrays and Frequency Band

The size of the sonar hydrophone array was selected to be 83 by 83 cm providing the array with spatial resolution that is identical for along track and across track directions. A large array size is desirable for scattering noise rejection and good spatial resolution. The maximum size was constrained by the need to operate the sonar from a small vessel and to mount the array on the front half of an AUV that has a length of 2 m or greater. The hydrophone elements are mounted on a 1×1 m acoustic baffle which blocks sea surface reverberation. Fig. 8 shows the sonar vehicle layout of the transmission line array consisting of six piston sources and a 32-channel planar hydrophone array. There are eight rows of hydrophones across the sonar vehicle where each row consists of four channels along the length of the vehicle. The four fore–aft channels in each row allow focusing in the same direction as the steering angle of the transmission beam. The eight rows of hydrophones allow control of focusing in the across track direction. The maximum number of channels was limited by the desire to use off-the-shelf components for processing and the limitation of 100BASE-T data transfer rates when sending 32 channels of 16 bit data sampled at 50 kHz from the sonar vehicle to the topside sonar processor.

The operating frequency band of 5–23 kHz was selected considering the following factors.

1) Wide bandwidth minimizes scattering noise interference.
2) Lowering the operating frequency reduces losses due to the high attenuation of sand (on the order of 1 dB/m/kHz).
3) Raising the operating frequency improves spatial resolution.
4) The maximum bandwidth of a piston source (Tonpilz resonator) is approximately two octaves.

The transmitted signal is a FM pulse with a pulse length of 2 ms. The acoustic returns are processed by a correlation processor to generate a sequence of subsurface reflections that resemble zero phase wavelets. The processed wavelet is shown in Fig. 9 and its amplitude spectrum, which is flat over the band of 5–23 kHz, is shown in Fig. 10. The correlation processor executes a filter which is a convolution of a matched filter and a filter that corrects for variations in the frequency spectrum of the sonar system over the band of 5–23 kHz.

C. System Overview

The buried object scanning sonar consists of a towed vehicle, a data and power cable, and a topside sonar processor. The towed vehicle contains the acoustic arrays and an underwater canister for transmitter and receiver electronics, data acquisition computer and motion sensor. A photo of the vehicle is shown in Fig. 11.

A block diagram of the software data flow structure is shown in Fig. 12. The system currently uses 7 Pentium processors. In the underwater canister, a Pentium II class computer along with two TMS320 DSP processor cards handle the real-time acquisition of 32 channels of hydrophone data and generate chirp pulses for the six acoustic projectors in the line array.

The acoustic transmitter consists of six piston sources, each driven by a separate 200 W linear power amplifier, and six dedicated 16-bit DACs, one for each transducer. The transmission beam can be steered by using a different, suitably delayed pulse for each transducer. The pulse memory supports up to eight transmission pulses for each of six transducers. When using more than one transmission angle, the distinct pulses, one for each angle, are cycled from pulse memory in round robin order. The number of transducers used to steer the outgoing pulse is adjusted to ensure the length of the transmission array is short enough to prevent destructive nearfield effects of the transmission beam when a target is close to the transmitter. If the vehicle altitude drops below approximately 3 m, the end elements of the transmission array will be deactivated to prevent transmitter nearfield problems allowing the sonar to operate at an altitude of 1 m while maintaining the full spatial processing gain of the nearfield receiver.

Each hydrophone input has a dedicated pre-amplifier, anti-aliasing low pass filter, and variable gain amplifier. There are eight 200-kHz 16-bit ADCs. Each ADC has a 1:4 input MUX
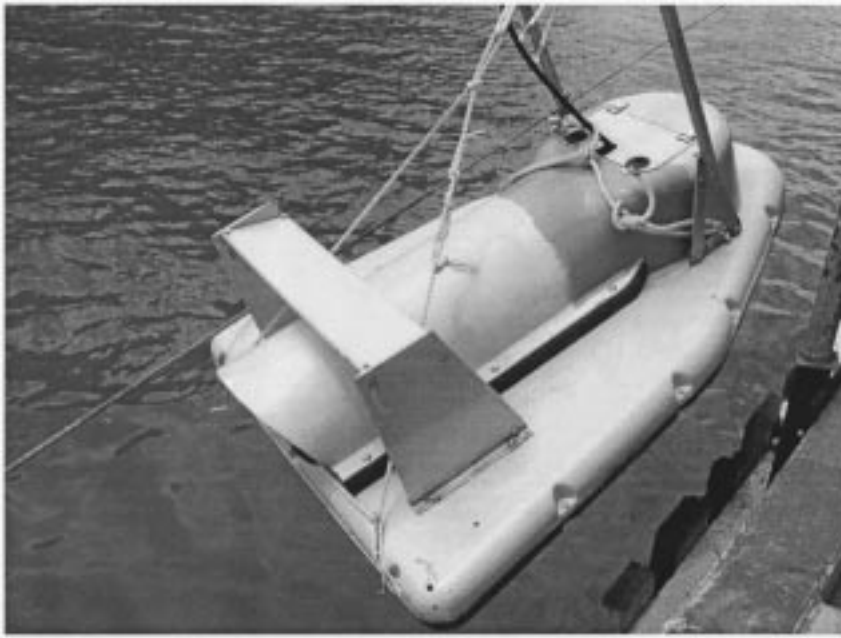
Fig. 11.   Photograph of sonar vehicle containing line transmitter, planar hydrophone array and underwater electronics canister.

and sample and hold circuitry. It takes four 200-kHz clock samples to digitize all 32 channels for an effective sample rate of 50 kHz per channel. Converted data is saved in the ADC data queue. The acquired data is sent over a 100BASE-T ethernet link to a surface computer for storage and display.

On the surface, the Sonar Control and Display Computer, a dual-processor Pentium III class computer, receives the digital data from the underwater canister in the sonar vehicle. This computer serves as the primary operator interface, including several sonar displays and a remote control console for the underwater canister. The main displays process, shown in Fig. 12, has several options including single channel waterfall, 2-D slice display, three-dimensional (3-D) view of the seabed including plan and side views, and a 3-D volume rendering of the seabed. The volume rendering display implements the MIP (maximum-intensity projection) algorithm that maps the seabed at any aspect to the 2-D viewing screen allowing the user to look through the seafloor at the buried targets [13]. This process also implements the automatic target detection algorithms. The sonar control and display computer also executes the record and playback process which is responsible for storing unprocessed receiver data on the local hard disk and replaying the data allowing simulation of real time acquisition and processing in the lab.

The beamformer process, which implements the focusing and correlation processing algorithms that generate the 2-D slice data from the raw sonar data, is the most computationally intensive part of the system. Two dual-processor computers, connected to the sonar control and display computer via 100 base T ethernet, perform the correlation processing and focusing calculations and send the 2-D slice data back to the sonar control and display computer for volume visualization of the targets in the seabed. Each dual processor runs two beamforming processes. Multiple beamformers can be used to enhance system throughput by assigning the 32-channel data set generated by a single ping to a beamformer process in a round-robin order so each beamformer is processing data from a different transmission. Since the sonar transmits 20 pulses per second, the beamformer must calculate 640 matched filters per second in addition to generating 2-D slices of focused data.

Finally, the surface rendering display process calculates the surface of the detected targets in a 3-D space using the marching cubes algorithm [13]. The operator controls surface rendering thresholds and can rotate the target to visualize its shape.

IV. RESULTS

A. Field Tests

The buried object scanning sonar was tested during the summer of 2000 at a test range setup by Sea Engineering, Inc. A set of objects including ordnance, pipes and a cable were buried in fine calcareous sands at the test range which is located along a pier on the east side of Oahu, HI. Most targets were buried at various aspect angles other than the trivial case of being parallel to the along track direction. Fig. 13 shows a drawing of the test field and Table I contains a description of the targets buried in the field and the submerged floats which provide acoustic markers of vehicle position. All targets were buried at least one month before collecting sonar data to allow the sediments to reach a natural condition thereby preventing disturbed sediments from generating false echoes at the target locations. Most targets had an overburden of approximately 30 cm of sand above the top of the target. The water depth along the test line varies from 4 to 5 m. The horizontal position was controlled by suspending the sonar vehicle under a trolley that rides on a wire rope suspended above the centerline of the test field. The depth of the sonar vehicle was constant during each test.

The tests were performed in a mode using two steering angles where successive pings would alternate between the two
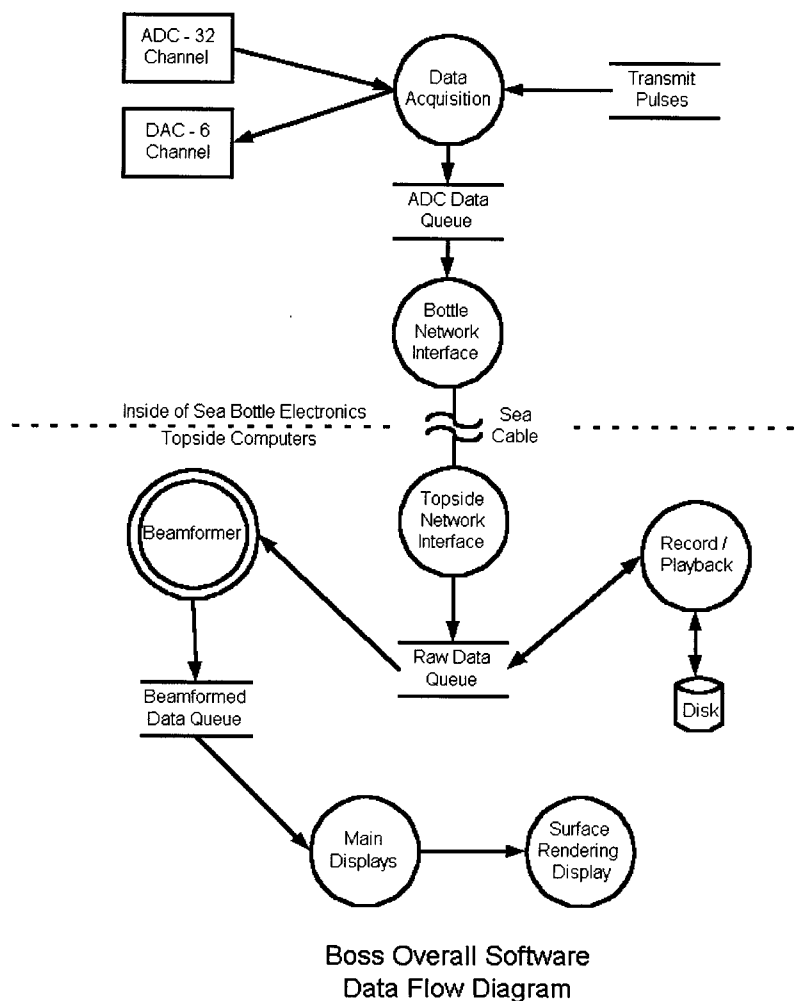
**Boss Overall Software
Data Flow Diagram**

Fig. 12. Data flow diagram for software running on seven Pentium processors in the buried object scanning sonar. The software provides real time 3-D focusing and volume visualization of the seabed structure and buried targets. In accordance with data flow notation, each circle represents a separate software process, a double circle represents multiple processes, two horizontal parallel lines indicate data storage and square box is an external interactor.
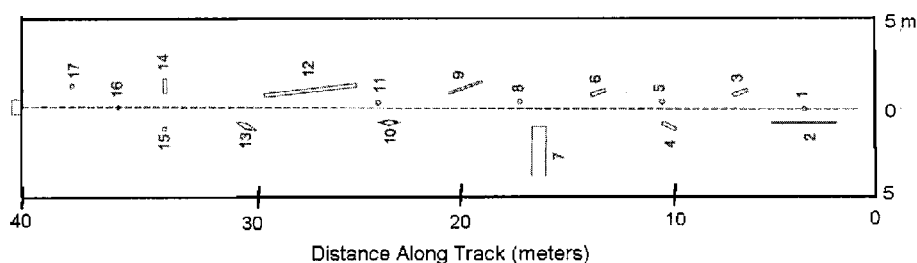

Fig. 13. Plan view of buried objects and submerged floats along the sonar testing line. The target descriptions are provided in Table I.

steering angles. This mode allowed us to compare the effect of steering angle on target imaging while maintaining a transmission rate of 10 pulses/s for each steering angle. Fig. 14 contains a side view and plan view of the field for steering angles of -13.1 and -8.7 deg. A negative steering angle indicates that the transmission beam is pointed behind the vehicle. The top display in both windows is a single channel waterfall. Note the improvement in the ratio of target echo to scattering noise when comparing a target echo in the single channel waterfall to the image of the same target in the two views generated from the focusing algorithm operating on 32 channels of data. The plan view displays only targets within 50 cm of the sediment–water interface to prevent the underlying sediment layering and coral basement from interfering with the imagery. The range of sub-surface depths used to construct the plan (top) view of the seabed is adjusted by the operator.

The displays in Fig. 14 demonstrate the importance of along track beamsteering. The comparison of the images of the iron and PVC pipes for the steering angles of -8.7 and -13.1 deg shows that a change in the beamsteering angle of 4.4 deg causes a large change in target SNR. As noted in Section II, small changes in the aspect of a buried cylinder cause large changes

TABLE I
DESCRIPTION OF TARGETS AND BURIAL DEPTHS VERIFIED BY DIVERS. THE PLAN VIEW OF THE TARGET FIELD IS SHOWN IN FIG. 13

| Target Number	Description	Thickness of sand over target + above seafloor, - below seafloor (cm)
8, 11	Air filled floats – various shapes	30
2	Double-armored cable, 3.8 cm diameter x 2.7 m long	-15
3, 4, 6, 14	Steel scuba tanks filled with concrete, 60 cm long x 17.5 cm diameter	-24 to −30
7	Thin walled pipe, 60 cm diameter, 30-90 cm above seafloor	30 to 90
9	PVC pipe, air filled, 8.7 cm diameter x 1.5 m long	-15
10, 13	155mm ordinance, 15 cm diameter x 90 cm long	-24 to −30
12	Ductile iron pipe, water filled, 15 cm diameter x 4 m long, 0.9 cm wall	-24 to −30
1, 5, 15, 16, 17	Air filled rubber balls, 20 cm diameter	30
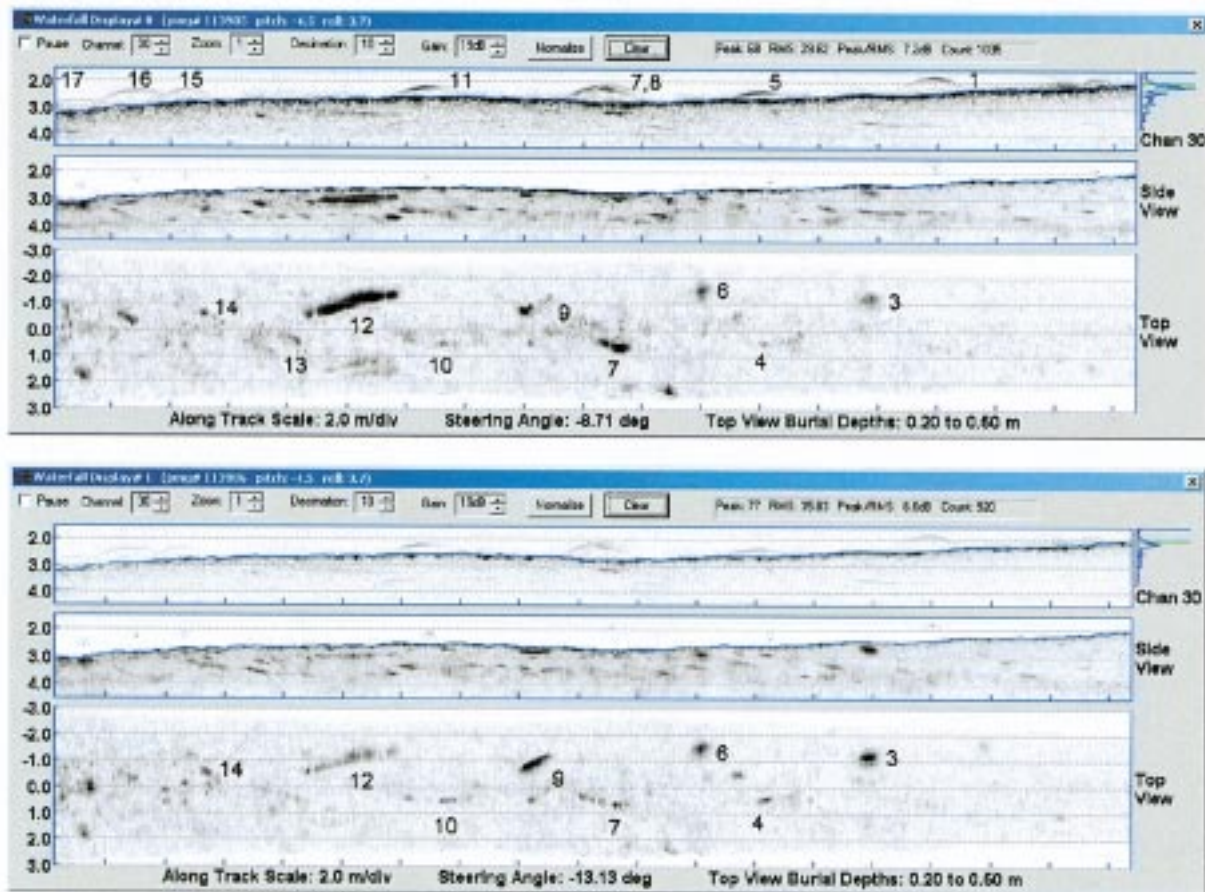
Fig. 14.   Sonar displays for transmitter steering angles of −8.7 and −13.1 deg. Each steering angle has three waterfall displays, one display for the correlated data from one hydrophone channel, and two displays showing the top and side views of the seabed generated from the 3-D matrix of focused data. The sonar started the run at the deep end of the test line. As the water depth decreased along the line, sonar height fell from 3 to 2 m.

in its target strength. Along track beamsteering is necessary to ensure adequate SNR for target imaging.

B. Measurements of System Performance

The SNR improvement of the 32-channel array can be estimated from single channel and focused images by comparing peak echo amplitudes and rms noise of scattering near the target echo. In theory if the noise is perfectly incoherent and the signal is perfectly coherent, the SNR improvement for a 32-channel array should be $10 \log 32$ or 15 dB. This improvement can be qualitatively seen when comparing the SNR of target echoes in the single channel waterfall and side view displays. Quantitative measurements of target SNR, given in Table II, show that the

TABLE II
COMPARISON OF TARGET SNR MEASURED BEFORE AND AFTER NEARFIELD FOCUSING. IF THE TARGET WAS NOT VISIBLE IN THE SIGNAL CHANNEL DATA, THE SNR WAS DENOTED NV IN THE TABLE. SINCE TARGETS CANNOT BE SEEN IN SIGNAL CHANNEL DATA WHEN SNR IS LESS THAN 6 DB, THE SNR IMPROVEMENT FOR TARGETS NOT VISIBLE IN THE SINGLE CHANNEL DATA IS AT LEAST THE SNR OF THE TARGET IN THE FOCUSED DATA MINUS 6 DB

| Target description	Target number	SNR (dB) based on best steering angle	SNR (dB) Single channel	SNR (dB) improvement from focusing 32 channels of data	Best steering angle (deg)	Actual target aspect (deg)
Cable	2	15	NV	>9	0	0 (parallel to track)
Water filled iron pipe	12	20	7	13	-8.7	16
Air filled PVC pipe	9	22	9	13	-13	22
Ordnance	10	16	NV	>10	-22	NA
Ordnance	13	18	NV	>12	-22	NA
Concrete filled steel cylinder	3	18	NV	>12	-13	NA
Concrete filled steel cylinder	4	16	10	6	8.7	NA
Concrete filled steel cylinder	6	17	NV	>11	-13	NA
Concrete filled steel cylinder	14	12	NV	>6	-8.7	90 (perpendicular to track)
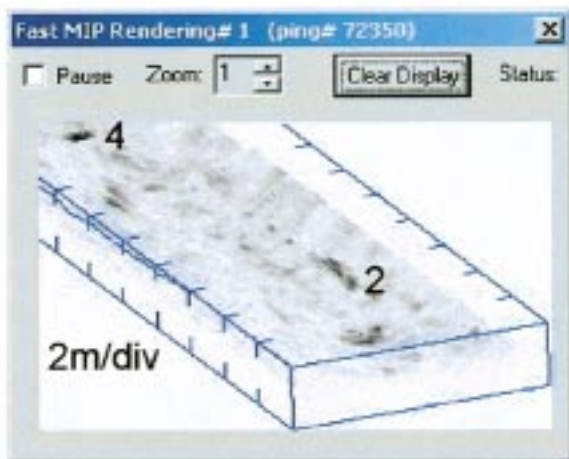
Fig. 15.   Volume rendering of the seabed using the maximum intensity projection algorithm. The steering angle is 8 deg. The volume display shows the buried cable section (target 2) and a concrete filled bottle (target 4). Other targets in the shallow end of the line cannot be seen using the steering angle of 8 deg. A blue line along the left-hand side of the display indicates the location of the detected seabed.

SNR improvement, generated by the focusing algorithm operating on the 32-channel data, is within 3 dB of the theoretical array gain of 15 dB for several targets.

The spatial resolution of the sonar can also be estimated from the images. The −3-dB widths of point targets in the along track and across track directions is approximately 10–20 cm which is substantially less than the dimensions of the 83 by 83 cm hydrophone array. Within the nearfield, angular spatial resolution depends on array size and bandwidth while temporal (range) resolution depends on bandwidth. Beyond the nearfield, the angular resolution (beamwidth) depends on array size and center frequency. 18 kHz of bandwidth provides a zero phase wavelet with a −3-dB width of 0.045 ms and a range resolution of 3–4

cm. The two octave bandwidth of the sonar is the major factor contributing to the high angular resolution in the nearfield.

A parameter called the focusing coefficient is also used to measure sonar performance. The focusing coefficient is measured for every pixel in the 2-D slice data to determine how accurately the sonar is focusing. The focusing coefficient is defined by

$$FC(y,z) = \frac{\left|\sum_{n=1}^{32} c_n(y,z)a_n(y,z)\right|}{\sum_{n=1}^{32} |c_n(y,z)a_n(y,z)|}. \tag{11}$$

If the receiving array data is in focus and $SNR \gg 0$ dB, the focusing coefficient calculated at the peak of a target echo is equal to one. In the side view display, pixels in the water column with focusing coefficients exceeding 0.97 are colored red. As expected, the red pixels in the water column correspond to the positions of the submerged floats. The red detections at float locations indicate that the sonar focusing is operating as designed.

C. Volume Visualization

Maximum intensity projection is used to generate volumetric views of the target field at various user view angles in real time. A pixel value in the volume visualization display is set equal to the maximum of the data samples encountered by a ray cast from the pixel location in the view plane through the 3-D matrix of 2-D seabed slices. An example of a volume rendering of the seabed volume can be seen in Fig. 15.

D. Target Detection

The sonar detects a buried target in real time by summing the energy of echoes reflected by the target over multiple transmissions and comparing the integral energy to an energy threshold. The integral energy is continuously calculated using N_P pings for each (y, z) position in the across track slice of the seabed.
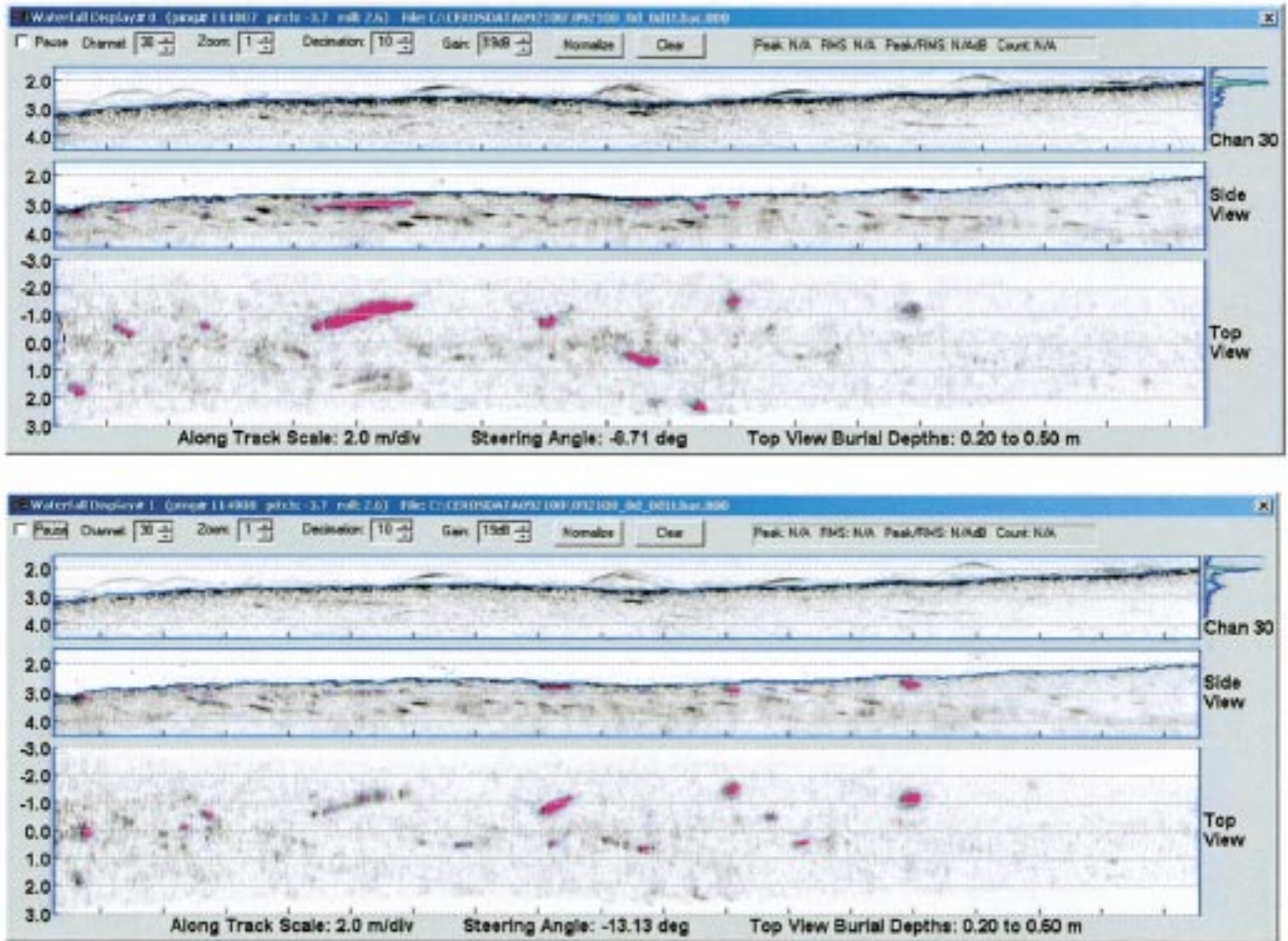
Fig. 16. Displays generated by the buried object scanning sonar with automatic target detection enabled. This display is identical Fig. 14 with the exception that the detections are colored red.

The integral energy calculated for ping number P and each position (y, z) is given by

$$E_P(y, z) = \sum_{p=P-N_P}^{P} A_p^2(y, z). \qquad (12)$$

Immediately after each transmission, the integral energy value is calculated for every pixel location in the 2-D slice and compared with the energy threshold. The threshold for the energy detector is set based on mission requirements for probability of detection and the acceptable number of false alarms for a given target of interest. Pixels associated with detections, events when the integral energy exceeds the energy threshold parameter, are colored red in the focused data display allowing the operator to monitor the performance of the filter. Automatic target detection provides the sonar with the ability to automatically store or display the (x, y, z) coordinates of buried targets.

With N_P set to six transmissions, the automatic detection algorithm was used to process the data displayed in Fig. 14. The pixels associated with the detections are colored red as shown in Fig. 16. Comparing Figs. 14 and 16, it is clear that all targets

shown in Fig. 14 (steering angles of -8.7 and -13.1) were detected with the exception of target 10 which was detected with steering angle of -22 deg. In addition, four unknown targets were detected. No false detections due to scattering noise appear in the selected data set for the steering angles of -13.1 and -8.7 deg.

V. CONCLUSION

The buried-object scanning sonar was developed to generate real time images of buried targets over a wide range of target aspect angles. The sonar uses a steerable transmission beam to minimize the scattering noise and to allow targets to be illuminated at various aspect angles. Low resolution images of cable and pipe sections, ordnance and cylinders buried approximately 30 cm in sand were generated in real time during field testing. After each transmission, a 2-D slice of the seabed is generated by performing near field focusing using the output of the 32-channel planar hydrophone array. The imagery is generated from a 3-D data matrix consisting of a sequence of 2-D slices of the seabed. Targets within the seabed volume are displayed using volume visualization at any viewer angle. Side and plan

views of the 3-D data matrix allow the operator to pinpoint the x, y and z positions of targets and to determine target orientation and size. An energy detection algorithm can be used to detect buried targets and report target information in real time.

ACKNOWLEDGMENT

REFERENCES

[1] J. E. Fernandez and J. T. Christoff, "Multi-aspect synthetic aperture sonar," in *Proc. IEEE OCEANS '00*, vol. 1, Sept. 2000, pp. 177–184.
[2] M. Neudorfer, J. Kosalos, and R. Bonneau, "Results of synthetic aperture sonar experiments," in *Proc. IEEE OCEANS '00*, vol. 1, Sept. 2000, pp. 323–330.
[3] H. Schmidt and J. Lee, "Physics of 3-D scattering from rippled seabeds and buried targets in shallow water," *J. Acoust. Soc. Amer.*, vol. 105, no. 3, pp. 1605–1617, 1999.
[4] A. Maguer, W. L. J. Fox, H. Schmidt, E. Pouliquen, and E. Bovio, "Mechanisms for subcritical penetration into a sandy bottom: Experimental and modeling results," *J. Acoust. Soc. Amer.*, vol. 107, no. 3, pp. 1215–1225, 2000.
[5] E. Thorsos, D. R. Jackson, and K. L. Williams, "Modeling of subcritical penetration into sediments due to interface roughness," *J. Acoust. Soc. Amer.*, vol. 107, no. 1, pp. 263–277.
[6] N. P. Chotiros, A. M. Mautner, A. Lovik, A. Kristensen, and O. Bergem, "Acoustic penetration of a silty sand sediment in the 1–10 kHz band," *IEEE J. Oceanic Eng.*, vol. 22, pp. 604–614, Oct. 1997.
[7] G. L. Sackman and G. R. Vermander, "Acoustic imaging in marine sediment: A multiple microprocessor array processor using the trace function," in *Acoustical Imaging*, J. P. Powers, Ed. New York: Plenum, 1982, vol. 11, pp. 225–243.
[8] S. A. Johnson, D. T. Borup, M. J. Berggren, J. W. Wiskin, and R. Eidens, "Modeling of inverse scattering and other tomographic algorithms in conjunction with wide bandwidth acoustic transducer arrays for towed or autonomous sub-bottom imaging systems," in *Proc. IEEE OCEANS '92*, Oct. 1992, pp. 294–299.
[9] R. J. Urick, *Principles of Underwater Sound*. New York: McGraw-Hill, 1983.
[10] W. S. Burdic, *Underwater Acoustic System Analysis*. Englewood Cliffs, NJ: Prentice-Hall, 1991.
[11] S. G. Schock, "Buried object scanning sonar," in *Proc. Oceanology Int.*, Brighton, U. K., Mar. 1998.
[12] S. G. Schock and L. R. LeBlanc, "Multi channel FM reflection profiler for buried pipeline surveying," in *Proc. Offshore Technology Conf.*, May 1996, pp. 659–665.
[13] A. Tellier, "Visualization of Buried Objects in 3D Acoustic Data Acquired by a Buried Object Scanning Sonar," M.Sc., Dept. of Ocean. Eng., Florida Atlantic University, Boca Raton, FL, Aug. 1999.
[14] L. E. Kinsler, A. R. Frey, A. B. Coppens, and J. V. Sanders, *Fundamentals of Acoustics*. New York: McGraw-Hill, 1982.

Steven G. Schock was born in Warwick, R.I., in 1956. He received the B.S. and Ph.D. degrees in ocean engineering, from the U. S. Naval Academy, annaplois, MD, and the University of Rhode Island, Kingston, RI, in 1979 and 1989, respectively.

He is currently an Associate Professor of Ocean Engineering at Florida Atlantic University, Boca Raton, where he has been conducting research and teaching since 1989. His research interests are bottom interacting acoustics, sediment classification, acoustic imaging and sonar design. He is a member of Acoustical Society of America and Marine Technology Society.

Arnaud M. Tellier was born in Montreuil, France, in 1974. He received the "Diplome d'Ingenieur de l'Ecole Centrale des Arts et Manufactures" from Ecole Centrale Paris, Chatenay-Malabry, France in 1997, and the M.S. degree in ocean engineering from Florida Atlantic University, Boca Raton, in 1999. He is currently a working toward the Ph. D. degree in the Department of Computer Science, Stanford University, Stanford, CA.

From 1998 to 2000, he was a Research Associate at Sea Engineering, Inc., Waimanalo, HI, where he developed and tested software for the buried object scanning sonar.

Jim Wulf was born in Miami, FL, in 1940. He received the B.S.E.E. degree from the University of Florida, Gainesville,1962.

He was with IBM Corporation from which he retired as a Senior Technical Staff Member. He joined the Department of Ocean Engineering at Florida Atlantic University, Boca Raton, in 1997, where he was the lead engineer for several sonar development projects.

Jason Sara (M'78) was born in Miami, FL, in 1959. He received the B.S., M.S., and Ph.D. degrees in electrical engineering in 1980, 1982, and 1984, respectively, from the Massachusetts Institute Of Technology, Cambridge, MA.

After graduation he joined United Technologies, Optical Systems Division, of WPB, FL where he developed adaptive optics signal processing systems. He joined EdgeTech of Milford, MA, in 1997 to develop high-resolution sub-bottom and side-scan sonar systems and currently serves as the lead software engineer.

Marc Ericksen was born in Palo Alto, CA, in 1961. He received the B.A. degree in earth sciences and the M.S. degree in marine geology, from Dartmouth College, Hanover, NH, and the Pennsylvania State University, State College, PA, in 1983, and 1987, respectively.

He has been a marine geologist with Sea Engineering, Inc., Waimanalo, HI, since 1991, specializing in marine geophysical, marine environmental and coastal studies.